

# Remote Magnetic Levitation Using Reduced Attitude Control and Parametric Field Models

Neelaksh Singh<sup>†</sup>, Jasan Zugaibi<sup>†</sup>, Denis von Arx, Bradley J. Nelson, and Michael Muehlebach

**Abstract**—Electromagnetic navigation systems (eMNS) are increasingly used in minimally invasive procedures such as endovascular interventions and targeted drug delivery due to their ability to generate fast and precise magnetic fields. In this paper, we utilize the OctoMag eMNS to achieve remote levitation and control of a rigid body across large air gaps which showcases the dynamic capabilities of clinical eMNS. A compact parametric analytical model maps coil currents to the forces and torques acting on the levitating object, eliminating the need for computationally expensive simulations or lookup tables and leading to a levitator agnostic modeling approach. Translational motion is stabilized using linear quadratic regulators. A nonlinear time-invariant controller is used to regulate the reduced attitude accounting for the inherent uncontrollability of rotations about the dipole axis and stabilizing the full five degrees of freedom controllable pose subspace. We analyze key design limitations and evaluate the approach through trajectory tracking experiments. This work demonstrates the dynamic capabilities and potential of feedback control in electromagnetic navigation, which is likely to open up new medical applications.

## SUPPLEMENTARY MATERIAL

A video of our work, with additional experiments not included in this paper, can be found at <https://youtu.be/2jLZ28T4uew>. The code accompanying this paper is available at [https://github.com/NeelakshSingh/oct\\_levitation.git](https://github.com/NeelakshSingh/oct_levitation.git).

## I. INTRODUCTION

Electromagnetic navigation systems (eMNS) are rapidly emerging as a promising technology in medical robotics, offering precise and responsive control over magnetic tools with applications ranging from endovascular interventions to targeted drug delivery [1]–[4]. Magnetic fields are generated either by moving permanent magnets [5] or by driving currents through electromagnets in an eMNS [6]. The former approach typically achieves higher field strengths and gradients, but the dynamic performance is limited by the inertia of the moving parts [7]. In contrast, eMNS typically have a significantly higher actuation bandwidth by rapidly modulating coil currents, making them more suitable for tasks requiring fast, closed-loop control.

<sup>†</sup>These authors contributed equally to this work.

Corresponding author: Jasan Zugaibi

\*This work was not supported by any organization

Neelaksh Singh, Jasan Zugaibi, Denis von Arx, and Bradley J. Nelson are with the Multi-Scale Robotics Lab, ETH Zürich, 8092 Zürich, Switzerland (e-mail: sneelaksh17@gmail.com; zjasan@ethz.ch; dvarx@ethz.ch; bnelson@ethz.ch).

Michael Muehlebach is with the Learning and Dynamical Systems Group, Max Planck Institute for Intelligent Systems, 72076 Tübingen, Germany (email: michael.muehlebach@tuebingen.mpg.de).

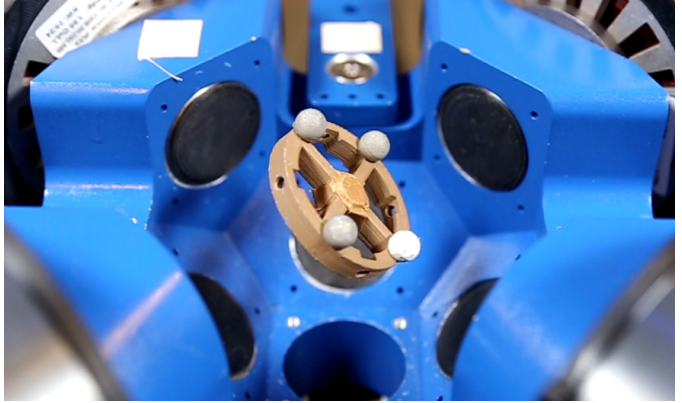


Fig. 1: A freely levitating object in OctoMag eMNS. The levitator's main body (bronze colored) was fabricated in a 3D printer using the Colorfabb BronzeFill® filament whose high density leads to high inertia with smaller dimensions to achieve more movement space in the OctoMag's small workspace. The dipole is made up of two N52 NdFeB disc permanent magnets ( $\varnothing 5$  mm  $\times$  10 mm each) that are symmetrically attached to the center of the levitator. Overall mass of the levitator is 32.4 g and its principal moments of inertia are  $(I_{xx}, I_{yy}, I_{zz}) = (6.21, 5.63, 1.14) \times 10^{-6}$  kg m<sup>2</sup>. A motion capture system detects three reflective markers attached to the levitator for pose estimation. The fourth marker, colored in white, is not reflective and just attached for achieving a symmetric weight distribution.

The literature on clinical electromagnetic navigation has largely focused on quasi-static modeling and open-loop control [8]–[10]. Recent research, however, argues that exploiting the available actuation bandwidth through feedback control significantly benefits procedures involving physiological motion, such as intracardiac ablation [11]. In addition, feedback control coupled with real-time state information enables an energy-efficient field allocation, increasing the workspace by up to an order of magnitude [12].

In this work, we further push the dynamic limits of eMNS by utilizing high-bandwidth feedback to achieve remote magnetic levitation of a centimeter-scale rigid body with the OctoMag eMNS [13], as illustrated in Fig. 1. Although the OctoMag is a research-grade platform typically associated with microrobotics and ophthalmic procedures [14], [15], we demonstrate its capacity for high-bandwidth control at a macroscopic scale. Establishing high-performance remote control of magnetic objects could pave the way for new medical applications since contactless manipulation inherently reduces friction, mechanical wear, backlash, and vibrations; characteristics that are undesirable for medical applications. For example, precise in-vivo levitation could enable diagnostic procedures such as detecting hidden tumors with sensorized ingestible capsules [16]. It could also improve colonoscopy, where magnetic actuation is already used to counteract gravity

and lift a soft-tethered capsule to reduce wall contact [17]. As clinical translation of our proposed framework relies on real-time state feedback, we emphasize the importance of high-frequency in-vivo state estimation techniques [18], [19].

To meet the listed requirements, as a proof of concept, we design a control and modeling framework to levitate rigid bodies. We first fit an analytical model relating electrical coil currents to the magnetic field within the workspace using calibration data. The resulting field is mapped to forces and torques using an analytical point-dipole representation. These field models are commonly used by the eMNS community as the main calibration tool [20]; however, to the best of our knowledge, this is the first time they are utilized to achieve macroscopic levitation of a permanent magnetic dipole in a physical experimental setup.

We deploy a nonlinear, time-invariant feedback controller that guarantees stability over all controllable orientations [21], [22]. This becomes particularly important in challenging in-vivo settings (e.g. magnetic capsule in intestine) where practical operation demands control across the levitator's full usable range of motion. However, for a symmetric rigid body with a single embedded magnetic dipole, rotations about the dipole axis are inherently uncontrollable [23]. Hence, we deploy a reduced attitude representation [24], that captures only the controllable attitude subspace.

In conclusion, this work makes three main contributions: First, we demonstrate, for the first time, remote magnetic levitation of a centimeter-scale rigid body in air using a clinical eMNS platform and extended working distances. Second, we use a levitator agnostic modeling strategy with an efficient calibration that allows straightforward reuse across different levitator designs. Third, we achieve stabilization and trajectory tracking over the full five degrees-of-freedom (DoF) controllable pose subspace. We evaluate our approach through trajectory tracking experiments and discuss important design considerations of the levitation system.

#### A. Related Work

Magnetic levitation itself has seen a surge of research activity in recent years. Many contributions have been driven by its use in precision motion systems [25], [26], maglev transport systems [27], [28], magnetic suspension [29], and contactless bearings [30]. However, remote magnetic levitation in air for biomedical applications has received comparatively little attention as most works focus on fluid-suspended magnetic bodies [1]. Only a few recent works explore remote magnetic levitation targeted towards biomedical settings [31]. Therefore, we mainly review advances in remote macroscopic magnetic levitation in air from non-medical domains that address the key challenges of large motion ranges and high-bandwidth control, which are important criteria for prospective clinical applications.

In the context of agile and high-range 5-6 DoF permanent magnet levitation, many works employ planar eMNS architectures that can be tiled to extend the horizontal workspace [23], [32]–[34]. In [23], a magnet is levitated using 10 cylindrical

coils arranged on a plane. Subsequent works [35], [36] build on this platform to demonstrate 6-DoF control of an object with two independent dipoles, simultaneous levitation of two such levitators, and omnidirectional control of a levitator with six spherically arranged permanent magnets. Similarly, [37] introduces a planar eMNS with square coils that simultaneously levitates a 2D Halbach array and an object with three magnets. The recently commercialized X-Planar® system by Beckhoff Automation allows fast 6-DoF control of platforms with magnet arrays with an unrestricted horizontal range [38]. In all these works, pose control is achieved through decoupled PID controllers which leads to a restricted range of stable attitudes. While the resulting motion range is sufficient for many industrial applications often dealing with controlled environments, clinical applications will require stabilization over a larger attitude range. Complex magnet configurations have been used to increase the range of stable attitudes in [36] with complex digital estimation and control. We instead rely on a simple single magnet levitator design and use a control scheme that leads to Lyapunov stability of almost the entire controllable attitude range.

A further distinction between previous works and our approach lies in the modeling paradigm. Existing high-range levitation systems predominantly identify or derive a direct map from coil currents to forces and torques on a specific levitator, often using force-torque sensors, levitator specific data collection rigs, and finite element analysis [23], [35], [39], [40]. This leads to models that must be re-identified whenever the levitator's magnet configuration changes. In contrast, the field-centric modeling strategy in this work decouples eMNS calibration from the specific magnet configuration, and, as long as independent magnet volumes remain small compared to the coil dimensions, new levitator designs can be accommodated by updating only their magnetic dipole parameters rather than re-identifying a full current to force-torque map.

#### B. Outline

The rest of this paper is organized as follows: Sec. II describes the experimental setup, defines all important quantities and notation, and gives a brief overview of the field model which relates coil currents to forces and torques on the levitating object. The dynamics of the levitator and control design are presented in Sec. III. Key performance considerations of the levitation system and the results from trajectory tracking experiments are discussed in Sec. IV. Finally, a conclusion is drawn in Sec. V.

## II. EXPERIMENTAL SETUP AND FIELD MODEL

This section describes the hardware setup used to develop and test the levitation pipeline. This is followed by an overview of the mathematical models governing the influence of coil currents on forces and torques applied to a permanent magnetic dipole.

#### A. Notation

Vectors are represented by bold lowercase letters, e.g.  $\mathbf{x}$ , and matrices are represented by bold uppercase or calligraphic

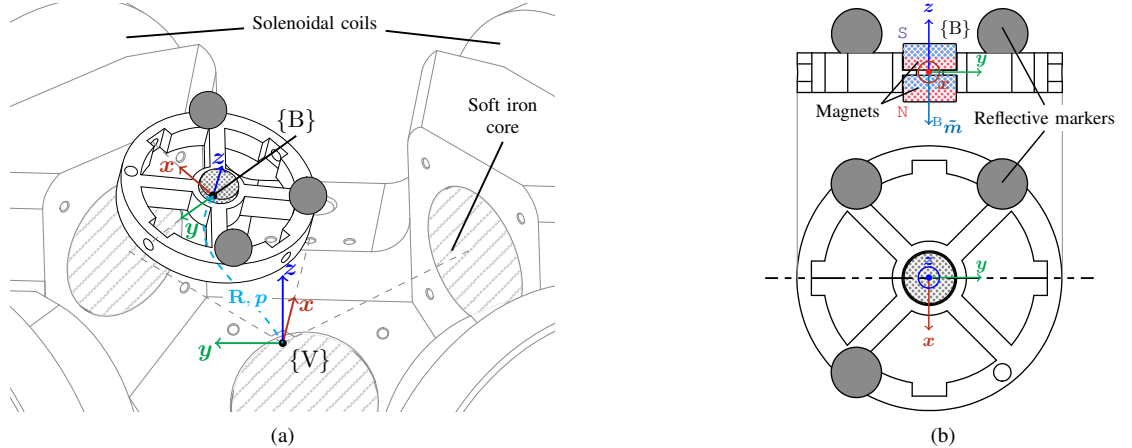


Fig. 2: Geometric notations and key components of the eMNS and the levitator. (a) The levitator's body frame  $\{B\}$  and the inertial world frame  $\{V\}$ . The OctoMag consists of eight solenoidal coils (approx.  $\varnothing 103 \text{ mm} \times 170 \text{ mm}$ ), each with a soft iron core, arranged in a spherical combination. The origin of  $\{V\}$  is located at the center of this sphere. Full pose of the levitator is provided as the rotation matrix  $\mathbf{R} \in \text{SO}(3)$  from  $\{B\}$  to  $\{V\}$ , and the position vector  $\mathbf{p} \in \mathbb{R}^3$  of  $\{B\}$  expressed in  $\{V\}$ . (b) The top and cross-section views of the levitator illustrating the placement of permanent magnets. Three reflective markers from Fig. 1 are shown in gray, while the non-reflective marker is not shown. The origin of  $\{B\}$  is approximately at the center of mass of the levitator. The two axially magnetized disc magnets used in the levitator are illustrated with a dot pattern. The net magnetic dipole moment of the assumed ideal point dipole in  $\{B\}$  is  ${}^B\vec{m} = -|\vec{m}|{}^B\mathbf{e}_z$ , since dipole moment is oriented from the magnet stack's overall south-pole (S) to the north-pole (N) by convention.

letters, e.g.  $\mathbf{X}$  or  $\mathcal{X}$ . We use two coordinate frames: the body-fixed frame referred to as  $\{B\}$ , and the inertial world frame referred to as  $\{V\}$ . Any vector  $\mathbf{x}$  resolved in  $\{B\}$  is denoted by  ${}^B\mathbf{x}$ , while all vectors without a frame superscript are expressed in  $\{V\}$ . The set of all normalized vectors in  $\mathbb{R}^3$  is the unit sphere represented by  $\mathbb{S}^2$ . The special orthogonal group, represented by  $\text{SO}(3)$ , is the set of rigid rotations in  $\mathbb{R}^3$ . We denote the standard unit vector along the  $z$  axis of any frame as  $\mathbf{e}_z = [0 \ 0 \ 1]^\top$ . Forces and torques are collectively referred to as a wrench, following standard convention in robotics.

### B. Experimental Setup

We employ the OctoMag eMNS, which comprises eight symmetrically arranged coils. Each coil consists of 1400 turns of laminated copper wire wound around a soft iron core. To achieve sufficient current controller bandwidth, a challenging task given the large coil inductance, we utilize custom-built drivers.

These drivers regulate coil currents using pulse-width modulated (PWM) voltages at a frequency of 20 kHz and an amplitude of 100 V. The effective bandwidth is characterized by the corner frequency ( $f_{\text{elec}}$ ), defined as the -3 dB point of the closed-loop response. This frequency determines the speed of current regulation and is a critical parameter in cascaded control architectures, where maximizing inner-loop bandwidth is generally desirable. Using the system identification method described in [11], we measured a corner frequency of  $f_{\text{elec}} = 26.4 \text{ Hz}$  at a current amplitude of 5 A. This value is significantly lower than those reported for smaller coils in related work [41], [42], underscoring the growing difficulty of achieving stable magnetic levitation as coil dimensions increase.

The levitator is 3D printed and contains two axially magnetized disc magnets at its center. Their physical parameters are summarized in Fig. 1, while Fig. 2 provides detailed

diagrams, including the relevant coordinate frames and key mechanical components. A motion-capture system with five tracking cameras operating at 1 kHz tracks the levitator's pose in real time by localizing three retro-reflective markers mounted on the levitator.

### C. Magnetic Field Model

The soft iron cores in OctoMag's coils exhibit negligible hysteresis effects [13]. We limit the current in each coil within  $\pm 4 \text{ A}$  so that the cores remain far from saturation. Therefore, the magnetic fields  $\mathbf{b} \in \mathbb{R}^3$  and gradients  $\mathbf{g} = [\partial b_x / \partial x \ \partial b_x / \partial y \ \partial b_x / \partial z \ \partial b_y / \partial y \ \partial b_y / \partial z]^\top \in \mathbb{R}^5$  at any position  $\mathbf{p} \in \mathbb{R}^3$  can be assumed to vary linearly with coil currents  $\mathbf{i} \in \mathbb{R}^8$  as follows

$$\begin{bmatrix} \mathbf{b} \\ \mathbf{g} \end{bmatrix} = \mathcal{A}(\mathbf{p}) \mathbf{i}, \quad (1)$$

where  $\mathbf{b}$ ,  $\mathbf{g}$ , and  $\mathbf{p}$  are expressed in  $\{V\}$  by convention [43]. The matrix-valued function  $\mathcal{A} : \mathbb{R}^3 \rightarrow \mathbb{R}^{8 \times 8}, \mathbf{p} \mapsto \mathcal{A}(\mathbf{p})$  is referred to as the actuation matrix. Note that there are only five independent gradient components for the magnetic field due to Maxwell's laws for quasi static fields in the absence of free currents ( $\nabla \cdot \mathbf{b} = 0$  and  $\nabla \times \mathbf{b} = 0$ ).

The actuation matrix is derived from the field model, with each column representing the field and gradient at position  $\mathbf{p}$  due to a unit current in the corresponding coil. Obtaining this model is the calibration step, which can be performed using various eMNS modelling methods [20], of which we use the Multipole Expansion Model (MPEM) [44]. MPEM is a parametric model derived from the analytical solution for cylindrically symmetric systems and models each coil as the multipole expansion of a point source with its magnetic center, orientation, and strength as parameters to be estimated. A simplified representation neglecting the higher order terms in the multipole expansion is sufficient due to the nominally

large air gaps between the coil cores and the levitator in this system. Therefore, for our purpose using only the dipole term is sufficient, and we assume that any modelling inaccuracies can be compensated through the feedback controller. This method requires only a few kilobytes of memory, can be computed offline via data-based parameter optimization, and can be queried in real-time to obtain  $\mathcal{A}(p)$  at any arbitrary position. Parameter optimization is performed using a least-squares fit to magnetic field measurements as described in [44]. Data was collected for various currents in each coil at 320 positions in  $\{V\}$  with a calibration cube comprising a  $4 \times 4 \times 4$  grid of Melexis MLX90393<sup>®</sup> hall sensors.

The levitator's magnetic volume is several orders of magnitude smaller than the dimensions of the electromagnets and the operating workspace so it can be approximated as an ideal point dipole at the magnetic volume's centroid which coincides with the levitator's center of mass as shown in Fig. 2b. The body frame torques  ${}^B\boldsymbol{\tau}$  and inertial frame forces  $\mathbf{f}$  acting on the point magnetic dipole can be computed as follows

$${}^B\boldsymbol{\tau} = {}^B\tilde{\mathbf{m}} \times {}^B\mathbf{b} = [{}^B\tilde{\mathbf{m}}]_{\times} {}^B\mathbf{b} = \mathbf{R}^T \mathbf{b} = \mathcal{M}_b \mathbf{b} \quad (2)$$

$$\mathbf{f} = (\tilde{\mathbf{m}} \cdot \nabla) \mathbf{b} \quad (3)$$

where  $[\cdot]_{\times}$  denotes the skew-symmetric matrix operator,  ${}^B\tilde{\mathbf{m}}$  is the magnetic dipole moment, and  $\mathbf{R}$  is the rotation matrix from  $\{B\}$  to  $\{V\}$ . The expression for force can be simplified as [45]

$$\mathbf{f} = \begin{bmatrix} m_x & m_y & m_z & 0 & 0 \\ 0 & m_x & 0 & m_y & m_z \\ -m_z & 0 & m_x & -m_z & m_y \end{bmatrix} \mathbf{g} := \mathcal{M}_g \mathbf{g}. \quad (4)$$

Hence, the overall map from the coil currents to the wrench acting on the levitating object can be expressed as

$$\begin{bmatrix} {}^B\boldsymbol{\tau} \\ \mathbf{f} \end{bmatrix} = \begin{bmatrix} \mathcal{M}_b & \mathbf{0}_{3 \times 5} \\ \mathbf{0}_{3 \times 3} & \mathcal{M}_g \end{bmatrix} \begin{bmatrix} \mathbf{b} \\ \mathbf{g} \end{bmatrix} = \mathcal{M}(\mathbf{R}, {}^B\tilde{\mathbf{m}}) \begin{bmatrix} \mathbf{b} \\ \mathbf{g} \end{bmatrix} = \mathcal{M}(\mathbf{R}, {}^B\tilde{\mathbf{m}}) \mathcal{A}(p) \mathbf{i} := \Lambda(\mathbf{R}, {}^B\tilde{\mathbf{m}}, p) \mathbf{i}, \quad (5)$$

where  $\mathcal{M} : \text{SO}(3) \times \mathbb{R}^3 \rightarrow \mathbb{R}^{6 \times 8}$  is known as the magnetic interaction matrix. We define the overall map from currents to wrench by  $\Lambda$ , which will be referred to as the allocation matrix. The functional dependence of  $\Lambda$ ,  $\mathcal{M}$ , and  $\mathcal{A}$  on the orientation  $\mathbf{R}$ , position  $p$ , and dipole moment  ${}^B\tilde{\mathbf{m}}$  is considered implicit in the notation and will be omitted in equations henceforth.

There is a zero row in  $[{}^B\tilde{\mathbf{m}}]_{\times}$  as magnetic fields cannot apply torques about the dipole axis, so  ${}^B\tau_z = 0$  for any set of coil currents. Therefore, we can consider a reduced map with the uncontrollable torque component removed as follows

$$\mathcal{M}_{b \sim z} = \begin{bmatrix} 0 & |{}^B\tilde{\mathbf{m}}| & 0 \\ -|{}^B\tilde{\mathbf{m}}| & 0 & 0 \end{bmatrix} \mathbf{R}^T \quad (6)$$

$$\bar{\Lambda} = \begin{bmatrix} \mathcal{M}_{b \sim z} & \mathbf{0}_{2 \times 5} \\ \mathbf{0}_{3 \times 3} & \mathcal{M}_g \end{bmatrix} \mathcal{A} = \mathcal{M}_{\sim z} \mathcal{A} \quad (7)$$

$$\begin{bmatrix} {}^B\boldsymbol{\tau}_{xy} \\ \mathbf{f} \end{bmatrix} = \bar{\Lambda} \mathbf{i}, \quad (8)$$

where  ${}^B\boldsymbol{\tau}_{xy} = [{}^B\tau_x \quad {}^B\tau_y]^T$ ,  $\mathcal{M}_{\sim z}$  is the reduced magnetic interaction matrix, and  $\bar{\Lambda}$  is the reduced allocation matrix. The dipole strength  $|\tilde{\mathbf{m}}|$  can be estimated by  $|\tilde{\mathbf{m}}| = b_r V / \mu_0$ , where  $b_r$  is the remanence of the magnet's material,  $V$  is the net magnetic volume, and  $\mu_0$  is vacuum magnetic permeability. As the levitator's mass increases, a larger magnetic volume with higher dipole strength is required to levitate while keeping currents within limits. This also applies when levitating close to the edges of the workspace where even small forces and torques can demand high currents [46]. However, an increase in the net magnetic volume means the ideal point dipole assumption becomes less accurate.

### III. DYNAMICS AND CONTROL

For all practical purposes, the levitator's velocity stays sufficiently small so that aerodynamic drag can be neglected. Then the dynamics of our levitator can be described as follows

$$\dot{\mathbf{p}} = \mathbf{v} \quad (9)$$

$$\dot{\mathbf{v}} = \frac{\mathbf{f}}{m} \quad (10)$$

$$\dot{\mathbf{R}} = \mathbf{R} [{}^B\boldsymbol{\omega}]_{\times} \quad (11)$$

$${}^B\dot{\omega}_x = \frac{I_{zz} - I_{yy}}{I_{xx}} {}^B\omega_y {}^B\omega_z + \frac{{}^B\tau_x}{I_{xx}} \quad (12)$$

$${}^B\dot{\omega}_y = \frac{I_{xx} - I_{zz}}{I_{yy}} {}^B\omega_x {}^B\omega_z + \frac{{}^B\tau_y}{I_{yy}} \quad (13)$$

$${}^B\dot{\omega}_z = \frac{I_{xx} - I_{yy}}{I_{zz}} {}^B\omega_x {}^B\omega_y \quad (14)$$

where  $\mathbf{v} \in \mathbb{R}^3$  is the levitator's linear velocity in  $\{V\}$ ,  ${}^B\boldsymbol{\omega} \in \mathbb{R}^3$  is its angular velocity expressed in  $\{B\}$ ,  $m$  its mass, and  $I_{xx}, I_{yy}, I_{zz}$  its principal moments of inertia [24]. Because the levitator is symmetric about the  $x$  and  $y$  axes ( $I_{xx} \approx I_{yy}$ ), the dynamics of  ${}^B\omega_z$  become inaccessible, preventing full attitude stabilization [47]. We can still stabilize a reduced version of the attitude which removes the uncontrollable rotation mode [22]. Note that  ${}^B\dot{\omega}_z \approx 0$  in the absence of disturbances and modelling uncertainties.

#### A. Feedback Controller Design

We use the definition of reduced attitude from [21], which is defined by choosing a fixed direction  ${}^B\hat{\mathbf{n}} \in \mathbb{S}^2$  in  $\{B\}$ . Then the reduced attitude  $\Gamma \in \mathbb{S}^2$  is defined as follows

$$\Gamma = \mathbf{R} {}^B\hat{\mathbf{n}}. \quad (15)$$

This representation disregards all rotations of the levitator about the axis  ${}^B\hat{\mathbf{n}}$ . We choose  ${}^B\hat{\mathbf{n}} = {}^B\mathbf{e}_z$ , which gives the following reduced attitude kinematics

$$\dot{\Gamma} = \left( \mathbf{R} \begin{bmatrix} {}^B\bar{\boldsymbol{\omega}} \\ 0 \end{bmatrix} \right) \times \Gamma, \quad (16)$$

where  ${}^B\bar{\boldsymbol{\omega}} = [{}^B\omega_x \quad {}^B\omega_y]^T$ . The reduced attitude  $\Gamma$  explicitly removes the inaccessible  ${}^B\omega_z$  component from the kinematics. A non-linear time-invariant controller is defined to stabilize the

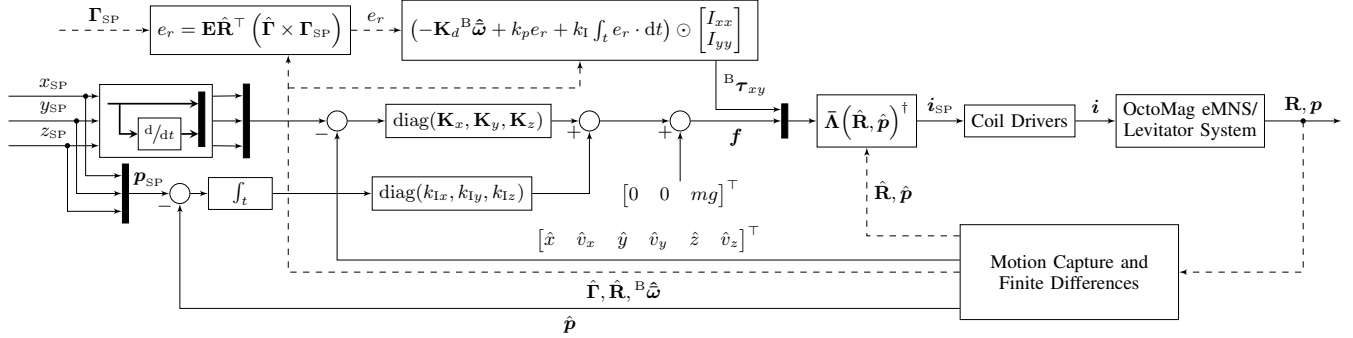


Fig. 3: Block diagram of the full levitation pipeline. All state variables with a  $\hat{\cdot}$  in the diagrams are states estimates from motion capture feedback and finite differences. Solid lines between blocks represent signals with linear gains and operations while dashed lines represent flow of information through non-linear function blocks. The solid black vertical bars represent column vector concatenation blocks.

reduced attitude to a desired value  $\mathbf{r}_{SP}$  with the two available torques as follows

$$\begin{bmatrix} {}^B\boldsymbol{\tau}_x \\ {}^B\boldsymbol{\tau}_y \end{bmatrix} = (-\mathbf{K}_d^B \hat{\boldsymbol{\omega}} + k_p \mathbf{ER}^\top(\mathbf{r} \times \mathbf{r}_{SP})) \odot \begin{bmatrix} I_{xx} \\ I_{yy} \end{bmatrix}, \quad (17)$$

where  $\mathbf{E} = \begin{bmatrix} 1 & 0 & 0 \\ 0 & 1 & 0 \end{bmatrix}$ ,  $\mathbf{K}_d \in \mathbb{R}^{2 \times 2}$ ,  $\mathbf{K}_d \succ 0$ ,  $k_p > 0$ ,  $\odot$  is the element-wise product, and  $\mathbf{K}_d$  and  $k_p$  are tuning parameters. Eq. (17) renders the closed-loop reduced attitude dynamics asymptotically stable about the desired equilibrium  $(\mathbf{r}_{SP}, 0)$  with a region of attraction that contains the entire state space except for the unstable antipodal equilibrium  $(-\mathbf{r}_{SP}, 0)$ ; see [21] for a formal analysis. Consequently, the controller can track any arbitrary setpoint  $\mathbf{r}_{SP} \in \mathbb{S}^2$  for all initial conditions except  $(\mathbf{r}_0, {}^B\boldsymbol{\omega}_0) = (-\mathbf{r}_{SP}, 0)$ .

The translational dynamics of the levitator are modeled as three decoupled double integrators, which gives rise to the following dynamics along the  $x$  axis for instance

$$\begin{bmatrix} \dot{x} \\ \dot{v}_x \end{bmatrix} = \begin{bmatrix} 0 & 1 \\ 0 & 0 \end{bmatrix} \begin{bmatrix} x \\ v_x \end{bmatrix} + \begin{bmatrix} 0 \\ \frac{1}{m} \end{bmatrix} f_x. \quad (18)$$

Let  $\mathbf{s}_x = [x \ v_x]^\top$  be the state along the  $x$ -axis. We discretize the dynamics using zero-order hold with the controller's sampling time  $T_s$  as

$$\mathbf{s}_x[k+1] = \mathbf{A}\mathbf{s}_x[k] + \mathbf{B}f_x[k]. \quad (19)$$

We further design a discrete-time LQR controller to compute the force  $f_x$  for regulating the state  $\mathbf{s}_x$  to a desired setpoint  $\mathbf{s}_{x,SP} = [x_{SP} \ v_{x,SP}]^\top$  as

$$f_x[k] = \mathbf{K}_x(\mathbf{s}_{x,SP} - \mathbf{s}_x), \quad (20)$$

where  $\mathbf{K}_x \in \mathbb{R}^2$  is the LQR gain matrix for the  $x$  axis. The same procedure applies to the  $y$  and  $z$  axes, and results in the LQR gain matrices  $\mathbf{K}_y, \mathbf{K}_z \in \mathbb{R}^2$ .

We compute the desired coil currents  $\mathbf{i}_{SP} \in \mathbb{R}^8$  from the desired wrench (Eqs. (17) and (20)) as

$$\mathbf{i}_{SP} = \bar{\Lambda}^\dagger \begin{bmatrix} {}^B\boldsymbol{\tau}_{xy} \\ \mathbf{f} \end{bmatrix}, \quad (21)$$

where  $\bar{\Lambda}^\dagger$  is the pseudoinverse of the reduced allocation matrix. These current setpoints are then sent to the coils' electrical

drivers which use a proportional integral (PI) controller for tracking the actual currents  $\mathbf{i}$ . Any inaccuracy in the field model, and thus  $\bar{\Lambda}$ , lead to input disturbances that cause steady-state errors despite inherent integrators in the dynamics. While high controller gains can reduce steady-state errors, they also amplify noise. To address this, we design integral actions,  ${}^B\boldsymbol{\tau}_{xy,I}$  for the reduced attitude controller and  $f_I$  for the translational controllers, as follows:

$${}^B\boldsymbol{\tau}_{xy,I} = \left( k_I \int_t e_r \cdot dt \right) \odot \begin{bmatrix} I_{xx} \\ I_{yy} \end{bmatrix} \quad (22)$$

$$f_I = \text{diag}(k_{Ix}, k_{Iy}, k_{Iz}) \int_t (\mathbf{p}_{SP} - \mathbf{p}) dt + \begin{bmatrix} 0 \\ 0 \\ mg \end{bmatrix}, \quad (23)$$

where  $k_I, k_{Ix}, k_{Iy}$  and  $k_{Iz}$  are integrator gains,  $\mathbf{p}_{SP}$  is the desired position, and  $e_r = \mathbf{ER}^\top(\mathbf{r} \times \mathbf{r}_{SP})$  is the error in reduced attitude. Note that a feedforward term for gravity compensation has been added to Eq. (23). Input disturbance due to model inaccuracies vary with the levitator's pose; therefore, the integral action must respond rapidly to remove steady-state offsets. Alternative disturbance estimation strategies for magnetic levitation systems have been proposed [48]–[51], but were not adopted here for simplicity. The resulting controller is shown in Fig. 3.

To achieve robust levitation, the pose controller's sampling time  $T_s$ , that is, the time period at which  $\mathbf{i}_{SP}$  updates are sent to the electrical drivers, is critical. The current drivers' PWM signals lead to ripples in the coil currents, which in turn lead to ripple fields; however, at the high switching frequency used here, these ripples do not affect the levitator due to its inertia. Consequently, the levitator is driven by the mean coil currents, so that between two successive sampling instants of the pose controller the actuating component of the magnetic field in the eMNS workspace can be regarded as effectively constant. During this interval, the levitator is unstable due to Earnshaw's theorem. As a consequence, if one tunes the controller gains to be robust against time delays by ensuring a certain phase margin without taking the magnetic field's effect into account, the actual tolerable delay will be much lower than predicted. The field's destabilizing effect can be modeled as a negative stiffness in the levitator's dynamics whose coefficient

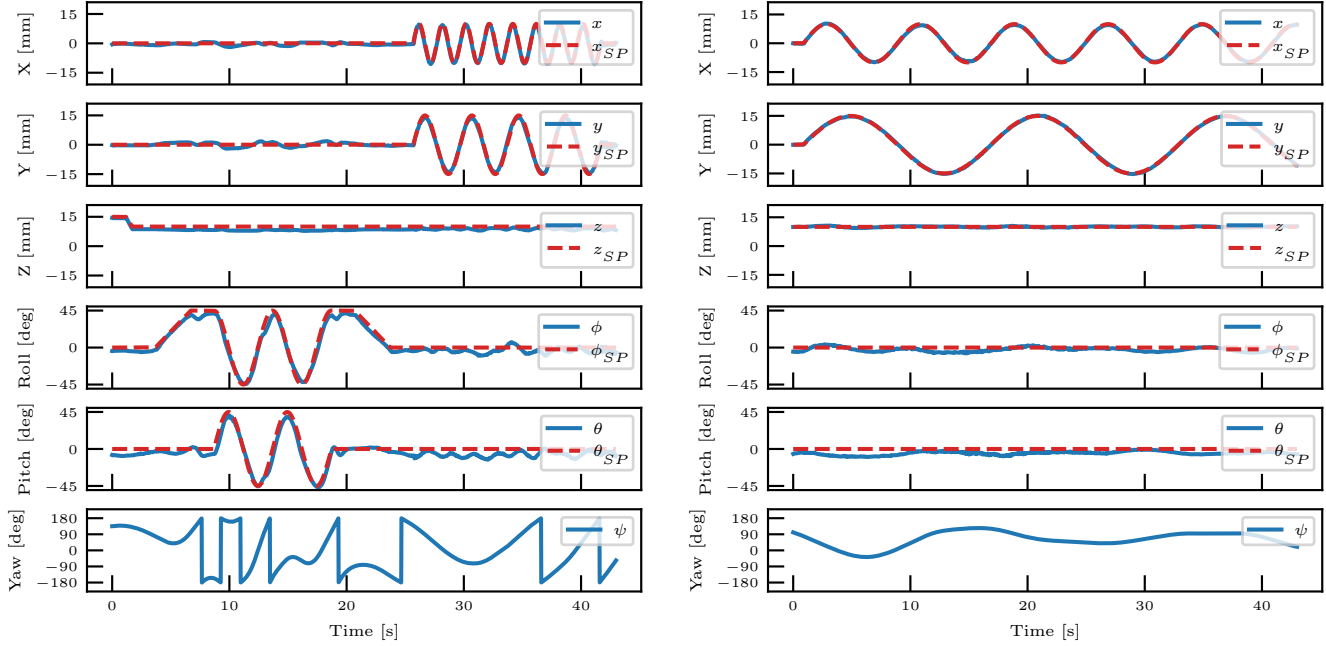


Fig. 4: Trajectory tracking experiments. Orientation is represented as XYZ intrinsic Euler angles: roll  $\phi$ , pitch  $\theta$ , and yaw  $\psi$ ; therefore, in this case  $\psi$  is the uncontrollable rotation mode. *Left*: Reference and actual pose of the levitator for a trajectory with large angles. The object tracks roll and pitch angles as high as  $\pm 45^\circ$  followed by figure eight maneuvers in the  $xy$ -plane without integrators. Gyroscopic coupling from imperfections in the levitator leads to large drifts in  $\psi$ . *Right*: Reference and actual pose for the figure eight trajectory with integrators enabled. Integrators remove the steady state error in  $z$ -setpoint tracking compared to the previous case. With minimal roll and pitch changes, gyroscopic coupling effects are negligible, so  $\psi$  shows less drift.

is inversely proportional to the controller sampling time  $T_s$  and changes spatially depending on the field model. Performing this analysis over the workspace may be used to estimate an upper bound on the effective degradation in phase margin as a function of  $T_s$  and is a direction for future work. This will be particularly useful for operating under low computational resources which do not allow for high sampling rates and when levitating lightweight bodies.

To conclude,  $T_s$  must be kept as low as possible. We operate pose controllers at 1 kHz, that is,  $T_s = 1$  ms which is fast enough to allow for stable levitation with simple controller tuning without explicitly modeling the field's destabilizing effect. Finally, note that rotations are more sensitive to noise and small field variations than translations. This is because the effective moments of inertia are significantly smaller than the mass, so even small disturbances can induce relatively large angular accelerations, making rotations the hardest to stabilize.

#### IV. RESULTS AND DISCUSSION

In this section, we evaluate our analysis through trajectory tracking experiments on the physical setup described in Sec. II-B.

Controllers are implemented in Python on Ubuntu 20.04 LTS, running on a 20-core 3.4 GHz Intel i7-14700HK CPU, and 64 GB of RAM. We use Robot Operating System (ROS) as the middleware for communication between software components. To reduce delays, parts of the code are just-in-time compiled and cached with Numba [52] reducing average computation times to less than 0.3 ms. The total delay, from

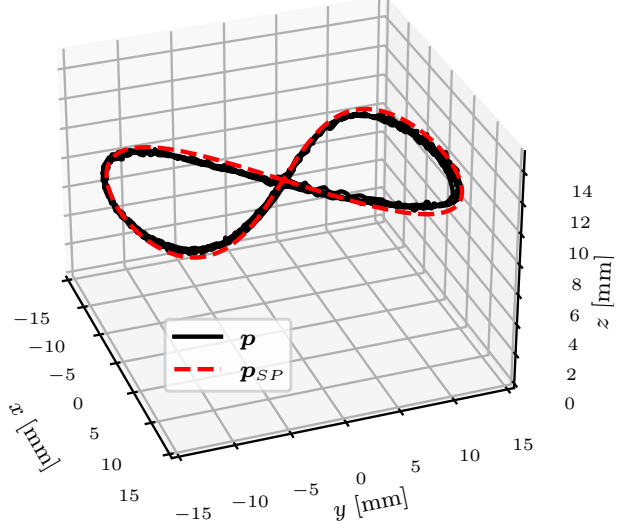


Fig. 5: 3D plot of reference and actual positions while tracking the  $xy$  figure eight trajectory with integrators enabled.

marker position acquisition to current setpoint arrival at the coil drivers, is approximately 4 ms. Since this is already four samples of delay for a controller operating at 1 kHz, it was crucial to ensure that the controller's computations were as fast as possible. Velocity estimates are obtained using first order backward finite differences.

We conducted the first trajectory tracking experiment without integrator action to demonstrate disturbance rejection capabilities of the base control pipeline. Fig. 4 on the left shows the

levitator tracking reference roll and pitch angles up to  $\pm 45^\circ$  followed by a figure-eight trajectory in the  $xy$ -plane. Most of the input-disturbance induced steady-state error is eliminated from proper controller tuning. Some steady-state error still persists, primarily in the  $z$ -axis, likely due to errors in the estimated object mass. In the second experiment, integrators were enabled to perform a similar  $xy$  figure-eight maneuver as shown on the right in Fig. 4. The integrator eliminates the steady-state error in  $z$ . A 3D plot of positions during this experiment is shown in Fig. 5. Imperfections in the object such as a non-diagonal inertia tensor lead to gyroscopic coupling in the dynamics of  ${}^B\omega_z$ ,  ${}^B\dot{\omega}_z$  and cause the yaw angle  $\psi$  to drift. Specific designs of the levitator's body and dipole placement may make the yaw dynamics accessible, which will make designing control laws for full attitude control with a single dipole possible [47]. The supplementary video presents further trajectory tracking experiments and demonstrates external disturbance rejection capabilities of our system.

For both experiments<sup>1</sup>, the linear integral gains were  $k_{Ix}, k_{Iy}, k_{Iz} = 10.0$  and the reduced attitude controller gains were  $\mathbf{K}_d = \text{diag}(108, 108)$ ,  $k_p = 472.5$ ,  $k_I = 100.0$ .

## V. CONCLUSION

This paper demonstrated stabilization and trajectory tracking of a levitating object with a permanent magnetic dipole using an eMNS. We used the OctoMag eMNS as the actuation platform, which was originally designed for minimally invasive eye surgeries. With this work, we aim to demonstrate the dynamic capabilities of eMNS - an important step toward clinical use cases, which are currently dominated by quasi-static models and feedforward control.

We modeled the magnetic field generated by the OctoMag's coil currents using MPEM, a parametric field model designed for computational efficiency. A stable feedback controller was synthesized to regulate the levitator's position and reduced attitude. Key design factors for achieving a robust performance, such as the choice of the levitator's mass, dipole moment, and the eMNS's bandwidth frequency were discussed. Experimental results showed that the system can perform rapid and accurate trajectory tracking, particularly at large rotation angles not reported before in the literature on magnetic levitation.

Our nonlinear reduced-attitude controller is currently constrained by the motion-capture system, which cannot track full rotations. Future work will extend the state estimation to handle full rotations and fully exploit the controller's performance. Another promising direction is to investigate whether levitation can be achieved on clinically ready, human-scale electromagnetic navigation systems such as Navion [6]. Our long-term goal is to push the limits of eMNS systems and

<sup>1</sup>For the LQR design, we normalize the state space as  $\bar{\mathbf{x}} = \mathbf{T}_x^{-1}\mathbf{x}$  and  $\bar{\mathbf{u}} = \mathbf{T}_u^{-1}\mathbf{u}$  for each axis. We choose  $\mathbf{T}_x = \text{diag}(\xi, 5\xi)$  and  $\mathbf{T}_u = 5m\xi$  where  $\xi = 5 \times 10^{-3}\text{m}$  is the nominal displacement value. The input cost coefficient is set to  $\mathbf{R} = 0.1$  for all three axes, and the state cost matrices are chosen as  $\mathbf{Q}_x = \text{diag}(22.0, 7.0)$ ,  $\mathbf{Q}_y = \text{diag}(15.0, 7.0)$ , and  $\mathbf{Q}_z = \text{diag}(30.0, 10.0)$ . LQR gain  $\bar{\mathbf{K}}$  obtained from the normalized system is then denormalized as  $\mathbf{K} = \mathbf{T}_u \bar{\mathbf{K}} \mathbf{T}_x^{-1}$ .

achieve highly complex, precise maneuvers that may enable new medical applications.

## ACKNOWLEDGMENT

The authors would like to thank Prof. Peter Berkelman from the University of Hawaii in Manoa for sharing valuable insights based on his years of experience in developing magnetic levitation systems. We also thank Felix Grüninger and Thomas Steinbrenner from MPI-IS Tübingen for their support with electronic and hardware designs essential to this project. Finally, we thank the team at MagnebotiX AG for technical support with the OctoMag eMNS.

## CONFLICT OF INTEREST

Bradley Nelson is a co-founder of MagnebotiX AG, which commercializes the OctoMag system. The other authors declare no conflict of interest.

## REFERENCES

- [1] S. R. Dabbagh, M. M. Alseed, M. Saadat, M. Sitti, and S. Tasoglu, "Biomedical Applications of Magnetic Levitation," *Advanced NanoBiomed Research*, vol. 2, no. 3, p. 2100103, 2022.
- [2] F. C. Landers, L. Hertle, V. Pustovalov, D. Sivakumaran, C. M. Oral, O. Brinkmann, K. Meiners, P. Theiler, V. Gantentein, A. Veciana, M. Mattmann, S. Riss, S. Gervasoni, C. Chautems, H. Ye, S. Sevim, A. D. Flouris, J. Puigmartí-Luis, T. S. Mayor, P. Alves, T. Lühmann, X. Chen, N. Ochsenbein, U. Moehrlen, T. Schubert, Z. Kulcsar, P. Gruber, M. Weisskopf, Q. Boehler, S. Pané, and B. J. Nelson, "Clinically ready magnetic microrobots for targeted therapies," *Science*, vol. 390, no. 6774, pp. 710–715, 2025.
- [3] Y. Kim, E. Genevriere, P. Harker, J. Choe, M. Balicki, R. W. Regenhardt, J. E. Vranic, A. A. Dmytriw, A. B. Patel, and X. Zhao, "Telerobotic neurovascular interventions with magnetic manipulation," *Science Robotics*, vol. 7, no. 65, p. eabg9907, 2022.
- [4] A. Mesot, M. Matttillé, Q. Boehler, N. Schmid, S. Lytle, F. Heemeyer, S. M. Chan, P. W. Y. Chiu, and B. J. Nelson, "Teleoperated magnetic endoscopy: A case study and perspective," *Advanced Intelligent Systems*, vol. 7, no. 10, p. 2400522, 2025.
- [5] J. W. Martin, B. Scaglioni, J. C. Norton, V. Subramanian, A. Arezzo, K. L. Obstein, and P. Valdastri, "Enabling the future of colonoscopy with intelligent and autonomous magnetic manipulation," *Nature Machine Intelligence*, vol. 2, no. 10, pp. 595–606, 2020.
- [6] S. Gervasoni, N. Pedrini, T. Rifai, C. Fischer, F. C. Landers, M. Mattmann, R. Dreyfus, S. Viviani, A. Veciana, E. Masina, B. Aktas, J. Puigmartí-Luis, C. Chautems, S. Pané, Q. Boehler, P. Gruber, and B. J. Nelson, "A human-scale clinically ready electromagnetic navigation system for magnetically responsive biomaterials and medical devices," *Advanced Materials*, vol. 36, no. 31, p. 2310701, 2024.
- [7] Z. Yang and L. Zhang, "Magnetic Actuation Systems for Miniature Robots: A Review," *Advanced Intelligent Systems*, vol. 2, no. 9, p. 2000082, 2020.
- [8] T. Liu and M. C. Çavuşoğlu, "Three dimensional modeling of an MRI actuated steerable catheter system," in *Proceedings of the IEEE International Conference on Robotics and Automation*, 2014, pp. 4393–4398.
- [9] J. Edelmann, A. J. Petruska, and B. J. Nelson, "Magnetic control of continuum devices," *The International Journal of Robotics Research*, vol. 36, no. 1, pp. 68–85, 2017.
- [10] C. Pappone, G. Vicedomini, F. Manguso, F. Gugliotta, P. Mazzzone, S. Gulletta, N. Sora, S. Sala, A. Marzi, G. Augello, L. Livolsi, A. Santagostino, and V. Santinelli, "Robotic magnetic navigation for atrial fibrillation ablation," *Journal of the American College of Cardiology*, vol. 47, no. 7, pp. 1390–1400, 2006.
- [11] J. Zugaibi, B. J. Nelson, and M. Muehlebach, "Dynamic Electromagnetic Navigation," *IEEE Robotics and Automation Letters*, vol. 10, no. 6, pp. 6095–6102, 2025.

[12] J. Zughabi, D. von Arx, M. Derungs, F. Heemeyer, L. A. Antonelli, Q. Boehler, M. Muehlebach, and B. J. Nelson, "Expanding the Workspace of Electromagnetic Navigation Systems Using Dynamic Feedback for Single- and Multi-agent Control," *arXiv*, 2025.

[13] M. P. Kummer, J. J. Abbott, B. E. Kratochvil, R. Borer, A. Sengul, and B. J. Nelson, "OctoMag: An Electromagnetic System for 5-DOF Wireless Micromanipulation," *IEEE Transactions on Robotics*, vol. 26, no. 6, pp. 1006–1017, 2010.

[14] F. Ulrich, C. Bergeles, J. Pokki, O. Ergeneman, S. Erni, G. Chatzipiridis, S. Pané, C. Framme, and B. J. Nelson, "Mobility Experiments With Microrobots for Minimally Invasive Intraocular Surgery," *Investigative Ophthalmology & Visual Science*, vol. 54, no. 4, pp. 2853–2863, 2013.

[15] H. Zhou, C. C. Mayorga-Martinez, S. Pané, L. Zhang, and M. Pumera, "Magnetically Driven Micro and Nanorobots," *Chemical Reviews*, vol. 121, no. 8, pp. 4999–5041, 2021.

[16] W. Chen, J. Sui, and C. Wang, "Magnetically Actuated Capsule Robots: A Review," *IEEE Access*, vol. 10, pp. 88398–88420, 2022.

[17] G. Pittiglio, L. Barducci, J. W. Martin, J. C. Norton, C. A. Avizzano, K. L. Obstein, and P. Valdastri, "Magnetic levitation for soft-tethered capsule colonoscopy actuated with a single permanent magnet: A dynamic control approach," *IEEE Robotics and Automation Letters*, vol. 4, no. 2, pp. 1224–1231, 2019.

[18] D. von Arx, C. Fischer, H. Torlakcik, S. Pané, B. J. Nelson, and Q. Boehler, "Simultaneous Localization and Actuation Using Electromagnetic Navigation Systems," *IEEE Transactions on Robotics*, vol. 40, pp. 1292–1308, 2024.

[19] M. Cavaliere, O. McVeigh, H. A. Jaeger, S. Hinds, K. O'Donoghue, and P. Cantillon-Murphy, "Inductive Sensor Design for Electromagnetic Tracking in Image Guided Interventions," *IEEE Sensors Journal*, vol. 20, no. 15, pp. 8623–8630, 2020.

[20] S. L. Charreyron, Q. Boehler, B. Kim, C. Weibel, C. Chautems, and B. J. Nelson, "Modeling Electromagnetic Navigation Systems," *IEEE Transactions on Robotics*, vol. 37, no. 4, pp. 1009–1021, 2021.

[21] N. Raj, L. J. Colombo, and A. Simha, "Structure preserving reduced attitude control of gyroscopes," *Automatica*, vol. 125, p. 109471, 2021.

[22] M. W. Mueller and R. D'Andrea, "Stability and control of a quadcopter despite the complete loss of one, two, or three propellers," in *Proceedings of the IEEE International Conference on Robotics and Automation*, 2014, pp. 45–52.

[23] P. Berkelman and M. Dzadovsky, "Magnet Levitation and Trajectory Following Motion Control Using a Planar Array of Cylindrical Coils," in *Proceedings of Dynamic Systems and Control Conference*. American Society of Mechanical Engineers Digital Collection, 2009, pp. 923–930.

[24] N. A. Chaturvedi, A. K. Sanyal, and N. H. McClamroch, "Rigid-Body Attitude Control," *IEEE Control Systems Magazine*, vol. 31, no. 3, pp. 30–51, 2011.

[25] Z. Zhang and C.-H. Menq, "Six-Axis Magnetic Levitation and Motion Control," *IEEE Transactions on Robotics*, vol. 23, no. 2, pp. 196–205, 2007.

[26] L. Zhou and J. Wu, "Magnetic Levitation Technology for Precision Motion Systems: A Review and Future Perspectives," *International Journal of Automation Technology*, vol. 16, no. 4, pp. 386–402, 2022.

[27] M. Kim, J.-H. Jeong, J. Lim, C.-H. Kim, and M. Won, "Design and Control of Levitation and Guidance Systems for a Semi-High-Speed Maglev Train," *Journal of Electrical Engineering and Technology*, vol. 12, no. 1, pp. 117–125, 2017.

[28] H.-S. Han and D.-S. Kim, *Magnetic Levitation*, Springer Tracts on Transportation and Traffic, 2016.

[29] H. Sawada, S. Suda, and T. Kunimasu, "NAL 60cm magnetic suspension and balance system," in *Congress of International Council of the Aeronautical Sciences*, 2004, pp. 2004–3.

[30] Z. Huang, C. Li, Z. Zhou, B. Liu, Y. Zhang, M. Yang, T. Gao, M. Liu, N. Zhang, S. Sharma, Y. S. Dambatta, and Y. Li, "Magnetic bearing: Structure, model, and control strategy," *The International Journal of Advanced Manufacturing Technology*, vol. 131, no. 5, pp. 3287–3333, 2024.

[31] W. Zheng, S. Deng, J. Chen, and S. Zou, "A low-power magnetic levitation capsule robot system based on permanent magnets-electromagnetic coils array," *AIP Advances*, vol. 15, no. 12, p. 125202, 2025.

[32] X. Lu and I. ur Rab Usman, "6D direct-drive technology for planar motion stages," *CIRP Annals*, vol. 61, no. 1, pp. 359–362, 2012.

[33] M. Dyck, X. Lu, and Y. Altintas, "Magnetically Levitated Rotary Table With Six Degrees of Freedom," *IEEE/ASME Transactions on Mechatronics*, vol. 22, no. 1, pp. 530–540, 2017.

[34] H. Zhu, T. J. Teo, and C. K. Pang, "Design and Modeling of a Six-Degree-of-Freedom Magnetically Levitated Positioner Using Square Coils and 1-D Halbach Arrays," *IEEE Transactions on Industrial Electronics*, vol. 64, no. 1, pp. 440–450, 2017.

[35] P. Berkelman and S. Kang, "Multiple Magnet Independent Levitation and Motion Control using a Single Coil Array," in *Proceedings of the International Conference on Advanced Intelligent Mechatronics*, 2023, pp. 537–542.

[36] M. Miyasaka and P. Berkelman, "Magnetic levitation with unlimited omnidirectional rotation range," *Mechatronics*, vol. 24, no. 3, pp. 252–264, 2014.

[37] Y. Wang and M. B. Khamesee, "MagFloor: A Universal Magnetic Levitation Platform for Flexible Manufacturing," in *2024 7th International Conference on Mechatronics, Robotics and Automation (ICMRA)*, 2024, pp. 152–156.

[38] L. Bentfeld, R. Brinkmann, P. Jebramcik, and T. Kaulmann, "Planar drive system," US Patent US12 289 022B2, Apr., 2025.

[39] Z. Xu, X. Zhang, and M. B. Khamesee, "Real-Time Data-Driven Force and Torque Modeling on a 2-D Halbach Array by a Symmetric Coil Considering End Effect," *IEEE Transactions on Magnetics*, vol. 58, no. 11, pp. 1–10, 2022.

[40] Y. Wang and M. B. Khamesee, "Deep Learning-Based Wrench Model for Magnetically Levitated Actuators," *IEEE Transactions on Industrial Electronics*, vol. 71, no. 11, pp. 14663–14672, 2024.

[41] P. Berkelman and M. Dzadovsky, "Magnetic Levitation Over Large Translation and Rotation Ranges in All Directions," *IEEE/ASME Transactions on Mechatronics*, vol. 18, no. 1, pp. 44–52, 2013.

[42] X. Zhang, C. Trakarnchaiyo, H. Zhang, and M. B. Khamesee, "MagTable: A tabletop system for 6-DOF large range and completely contactless operation using magnetic levitation," *Mechatronics*, vol. 77, p. 102600, 2021.

[43] A. J. Petruska and B. J. Nelson, "Minimum Bounds on the Number of Electromagnets Required for Remote Magnetic Manipulation," *IEEE Transactions on Robotics*, vol. 31, no. 3, pp. 714–722, 2015.

[44] A. J. Petruska, J. Edelmann, and B. J. Nelson, "Model-Based Calibration for Magnetic Manipulation," *IEEE Transactions on Magnetics*, vol. 53, no. 7, pp. 1–6, 2017.

[45] J. J. Abbott, E. Diller, and A. J. Petruska, "Magnetic Methods in Robotics," *Annual Review of Control, Robotics, and Autonomous Systems*, vol. 3, no. Volume 3, 2020, pp. 57–90, 2020.

[46] Q. Boehler, S. Gervasoni, S. L. Charreyron, C. Chautems, and B. J. Nelson, "On the Workspace of Electromagnetic Navigation Systems," *IEEE Transactions on Robotics*, vol. 39, no. 1, pp. 791–807, 2023.

[47] H. Krishnan, M. Reyhanoglu, and H. McClamroch, "Attitude stabilization of a rigid spacecraft using two control torques: A nonlinear control approach based on the spacecraft attitude dynamics," *Automatica*, vol. 30, no. 6, pp. 1023–1027, 1994.

[48] Y.-S. Lu and P. and Berkelman, "Design and Evaluation of State and Disturbance Observers for a Multivariable Magnetic Levitation System," *IETE Journal of Research*, vol. 69, no. 1, pp. 420–437, 2023.

[49] X. Wu, K. Xu, Q. Lu, H. Dong, G. Huang, and D. Zhang, "Disturbance Rejection Control for Magnetic Levitation System with Nondifferentiable Uncertainties and Measurement Noise," *IEEE Transactions on Instrumentation and Measurement*, vol. 74, pp. 1–11, 2025.

[50] J. Wang, L. Chen, and Q. Xu, "Disturbance Estimation-Based Robust Model Predictive Position Tracking Control for Magnetic Levitation System," *IEEE/ASME Transactions on Mechatronics*, vol. 27, no. 1, pp. 81–92, 2022.

[51] J. Wang, Q. Jiang, and H. Wang, "Generalized Disturbance Estimation Based Continuous Integral Terminal Sliding Mode Control for Magnetic Levitation Systems," *IEEE Transactions on Automation Science and Engineering*, vol. 22, pp. 1725–1737, 2025.

[52] S. K. Lam, A. Pitrou, and S. Seibert, "Numba: A LLVM-based Python JIT compiler," in *Proceedings of the Second Workshop on the LLVM Compiler Infrastructure in HPC*. Association for Computing Machinery, 2015, pp. 1–6.